JOURNAL OF MATERIALS SCIENCE 29 (1994) 4567–4576

Response of aluminium-infiltrated boron carbide cermets to shock wave loading

W. R. BLUMENTHAL*, G. T. GRAY III*, T. N. CLAYTOR‡
*Materials Science and Technology Division, ‡Design Engineering Division,
Los Alamos National Laboratory, Los Alamos, NM 87545, USA

Shock-recovery and shock-spallation experiments were performed on two compositions of aluminium-infiltrated B_4C cermets as a function of shock pressure. Sixty-five per cent volume B_4C–Al cermets were recovered largely intact after shock loading up to pressures of ca. 12 GPa which permitted a critical study of the microstructural changes produced by the shock. Significantly, shock loading to between 12 and 13 GPa produced a combination of dislocation debris, stacking faults and deformation twins in a small fraction of the B_4C grains. Fragmentation of shock-loaded 80% B_4C–Al samples prevented meaningful microstructural investigation. Spall-strength testing also provided indirect evidence for the Hugoniot elastic limits (HEL) of these composites. Spall-strength calculations based on an elastic equation of state for 65% B_4C–Al indicated that the elastic regime extended up to shock pressures of ca. 10 GPa, or approximately 65% of the HEL of polycrystalline B_4C. A complete loss of spall strength was then observed at the transition to a plastic equation of state at a pressure of 12 GPa which coincided with observations of plasticity within the B_4C-substructure. This study demonstrated that composites containing a highly ductile phase combined with a high compressive strength ceramic phase could support high dynamic tensile stresses by resisting the propagation of catastrophic cracks through the brittle ceramic substructure.

1. Introduction

The propagation of plastic shock waves through metals is known to induce widespread microstructural changes (i.e. dislocations, twins, phase transformation products, etc.) which differ from those observed when equivalent amounts of deformation are applied at lower strain rates. Consequently, constitutive relations describing the deformation of ductile materials must account for this strain rate dependence.

Uniaxial stress loading of dense, isotropic brittle materials at quasi-static strain rates produces an elastic response followed immediately by catastrophic failure from the propagation of cracks through the sample. Inelastic processes occur in only a tiny fraction of the sample volume (normally associated with the initiation and propagation of cracks at pre-existing flaws) and generally occur only at the instant before failure, so that deviations from elasticity are not observed by low strain rate diagnostic techniques. Loading at high strain rates has been postulated to suppress activation of relatively large strength-limiting flaws due to inertia. These inertial effects allow secondary cracks to initiate and propagate from less severe microstructural defects. Brittle geologic materials have been shown to have strengths which increase at moderate strain rates (10^2–10^4 s^{-1}) in uniaxial tension due to their large and broad flaw populations [1]. As a consequence of the activation of a higher fraction of the flaw population there is a decrease in the average fragment size with increasing strain rate.

Very high strain rates ($> 10^5$ s^{-1}) can be achieved in brittle materials using high-velocity-plate-impact to produce shock loading. Instead of a uniaxial stress state, ideal shock loading produces a uniaxial strain state of relatively short duration. Intense transverse pressure must develop to maintain transverse strains equal to zero. These confining pressures suppress crack propagation and can also extend the elastic response to higher axial stress levels. The stress level defining the transition to inelastic deformation is commonly referred to as the Hugoniot elastic limit (HEL). This onset of inelastic behaviour in brittle materials is typically equated to the onset of plasticity in metals. Recent work on ceramics by Kipp and Grady [2] at relatively high peak shock pressures found the HEL of titanium diboride and silicon carbide to be over 50% greater than previous measurements. Earlier studies generally used lower peak shock pressures, dissimilar impact designs and different diagnostic techniques. Kipp and Grady [2] also observed a broad range of mechanical responses following attainment of the HEL for various ceramics indicating that inelastic deformation of brittle materials is complex and difficult to generalize.

A large number of microstructural studies have been performed on metallic systems subject to shock

0022–2461

loading [3]. However, only a limited number of brittle materials have been studied by applying shock-recovery techniques originally developed for metals. The majority of these shock-recovery studies have concentrated on minerals [4–6] and monolithic ceramics [7–9]. Microstructural studies on shock-recovered minerals (quartz, anorthite and periclase) have revealed planar features, "shock lamallae", implying inhomogeneous local plastic flow above the HEL as suggested by Grady [5]. Conversely, transmission electron microscopy (TEM) examination of shock-recovered olivine by Jealoz [6] found no evidence of shear bands or zones of high local temperatures. Louro [9] showed that grain boundary flaws and cracking can lead to fragmentation of polycrystalline ceramics at compressive shock pressures below the HEL, and Brusso *et al.* [7] observed considerable fragmentation in alumina at a pressure of 20 GPa. Impact loading of alumina by Brusso *et al.* [7] and titanium diboride (TiB_2) by Vanderwalker and Croft [8] has also shown that a high density of dislocations, and, in the case of TiB_2, a large number of point defects, are produced as a result of shock loading.

The primary reason for the absence of microstructural studies on shock-loaded brittle materials is that at shock pressures large enough to be of interest, samples fragment to the extent that microstructural analysis cannot distinguish between shock and post-shock fragmentation effects. This fragmentation is often the result of impedance mismatch in the shock-recovery fixtures. The performance and integrity loss associated with ceramic fragmentation is the main motivation for developing high fracture toughness ceramic–metal (cermet) composites for impact applications.

Therefore, the objectives of this study were to: 1. apply advanced shock-recovery techniques to several compositions of boron carbide–aluminium cermets – it was expected that these techniques would minimize sample fragmentation and enable detailed microstructural characterization as a function of peak shock pressure; and 2. investigate the spall strengths of the cermets as a function of initial compressive shock pressure.

2. Materials

Two high-volume-fraction boron carbide–aluminium cermets were fabricated at the University of Washington by Drs Ilhan Aksay and Dave Millius. Pure liquid aluminium was infiltrated at ca. 1175°C into partially sintered, open porosity, boron carbide preforms having relative densities of 65 and 80%. This process produced near-theoretically dense (less than 2% residual porosity), isotropic, strongly-bonded and dual-continuous phase ceramic–metal composites. Quantitative metallography of polished sections were used to determine the average boron carbide phase size as 6 and 18 μm for the 65 and 80% B_4C compositions, respectively. The average aluminium phase size was found to be much finer at ca. 2 μm for both compositions.

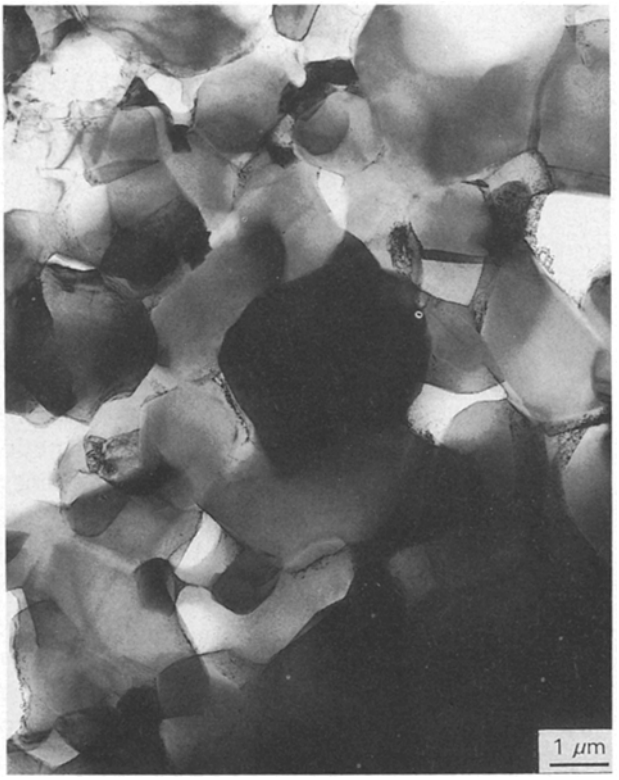

Figure 1 TEM bright-field of as-received 65% B_4C–Al reveal a nearly defect-free and twin-free boron carbide substructure with only occasional stacking faults.

TABLE I Cermet quasi-static properties

Property	Cermet Composition	
	65% B_4C–Al	80% B_4C–Al
Flexure strength, 4-PT (MPa) [10]	624	530
Fracture toughness (MPa $m^{1/2}$) [10]	9.5	8.1
Density (g cm^{-3})	2.570 ± 0.003	2.536 ± 0.004
Longitudinal sound speed (km s^{-1})	10.63 ± 0.02	12.20 ± 0.02
Shear sound speed (km s^{-1})	6.24 ± 0.01	7.40 ± 0.01
Poisson ratio–ultrasonic	0.24 ± 0.005	0.21 ± 0.005
Young's modulus – ultrasonic (GPa)	247 ± 1.5	335 ± 2.5
Secant modulus at 1% strain (GPa)	151 ± 2.5	315 ± 2.5
Compressive strength at 10^{-3} s^{-1} (MPa)	1935 ± 96	4000 ± 150

The as-received material was characterized using TEM as shown in Fig. 1. A nearly defect-free and twin-free boron carbide substructure was observed with only occasional stacking faults. The aluminium substructure was difficult to discern because it had been preferentially removed during preparation, but it contained a low density of dislocations and appeared well-bonded to the B_4C phase. The defect density in the aluminium was consistent with dislocations generated at the B_4C–aluminium interface on cooling due to the mismatch in their thermal expansion coefficients. Table I summarizes key quasi-static physical properties for these two cermets.

3. Experimental procedures

3.1. Spall testing

Spall-strength experiments were performed using an 80 mm diameter bore single-stage gas gun. Cermet samples, 18 mm in diameter by 2.3 mm thick, were placed within a set of concentric titanium alloy momentum trapping rings. A 3.5 mm^2 nominally 49 Ω manganin foil pressure gauge (Micro-Measurements, Inc Raleigh, NC), was epoxy-bonded into a shallow slot on the surface of a 9.5 mm thick polymethyl methacrylate (PMMA) holder, covered with a 0.8 mm PMMA sheet.

The PMMA holder was simultaneously epoxy-bonded to the sample so that the manganin gauge was located directly behind the centre of the sample. The PMMA served as a "witness" material within which shock pressures could be measured directly. The magnitude of the stresses in the cermet samples were then calculated based on the cermet equation-of-state defined in section 3.2 (Table II) and a linearized equation-of-state for PMMA (ambient density = 1.186 g cm^{-3}) : $U_s = 2.94 + 0.92U_p$ ($km\,s^{-1}$) [11, 12]. Sample assemblies were impacted with nominally 1.1 mm thick titanium alloy flyer plates at velocities of between 600 and 1107 $m\,s^{-1}$ with the intention of measuring the spall strength as a function of peak shock pressure.

The spall strength was calculated from the magnitudes of the peak and pull-back gauge resistances, the appropriate equations-of-state and a resistance correction for plastic shocks, which accounted for the truncation of the pull-back gauge resistance by the faster release wave (no correction was applied to elastic shocks). These procedures have been described in detail elsewhere [13].

3.2. Shock recovery

Shock-recovery experiments were performed using an 80 mm single-stage gas gun (Fig. 2) to preserve shock-induced microstructures. Cermet samples, 18 mm in diameter by 3.8 mm thick, were first sandwiched between two 1.4 mm cover plates, also made from the cermet. The cover plates were designed to protect the central sample from axial release waves. The sandwich was placed 2.5 mm from the impact end of a precisely machined 38 mm diameter by 19 mm high titanium alloy (Ti–6Al–4V) container. The container was closed from the rear and the sample was placed under slight compression with a threaded plug torqued to 27 N m to minimize free volume. For higher velocity impacts (> 1 $km\,s^{-1}$), samples were also protected from radial release waves by a split cermet trapping ring which surrounded the sandwich within the titanium container (outer diameter = 25 mm). The Ti–6Al–4V container was then backed by a 38 mm diameter by 6 mm thick spall plate and surrounded by two concentric momentum trapping rings with outer diameters of 70 and 80 mm, respectively. The momentum-trapping components were all made from Ti–6Al–4V to minimize shock impedance mismatch. Impedance values of 2.3, 2.0 and 2.2 $g\,cm^{-2}\,s^{-1}$ were calculated for Ti–6Al–4V, 65% B_4C–Al and 80% B_4C–Al materials, respectively, using bulk sound velocities and ambient densities.

Shock pressures and spall strengths were calculated using the constitutive equations presented in Table II, which assumed that the shock was either elastic (i.e. up to the HEL) or was dominated by the plastic component of the wave (i.e. well above the HEL). The elastic equations-of-state equate shock velocity, U_s, to the ultrasonically-measured longitudinal sound speed of the cermets with no dependence on the particle velocity, U_p. A rule-of-mixtures (ROM) estimate was used to calculate both the slope and intercept of the plastic $U_s - U_p$ relationships. $U_s - U_p$ slopes of 1.0 [2] and 1.34 [11], and intercepts of 9.65 and 5.38 $km\,s^{-1}$ were used for pure polycrystalline B_4C and pure aluminium, respectively.

Sample assemblies were impacted with nominally 3.0 mm thick Ti–6Al–4V alloy flyer plates in order to generate ca. 1 μs shock pulse. Impact velocities of 500 and 1023 $m\,s^{-1}$ were used to produce peak shock amplitudes in the range of 5.7 (plastic) to 6.4 GPa

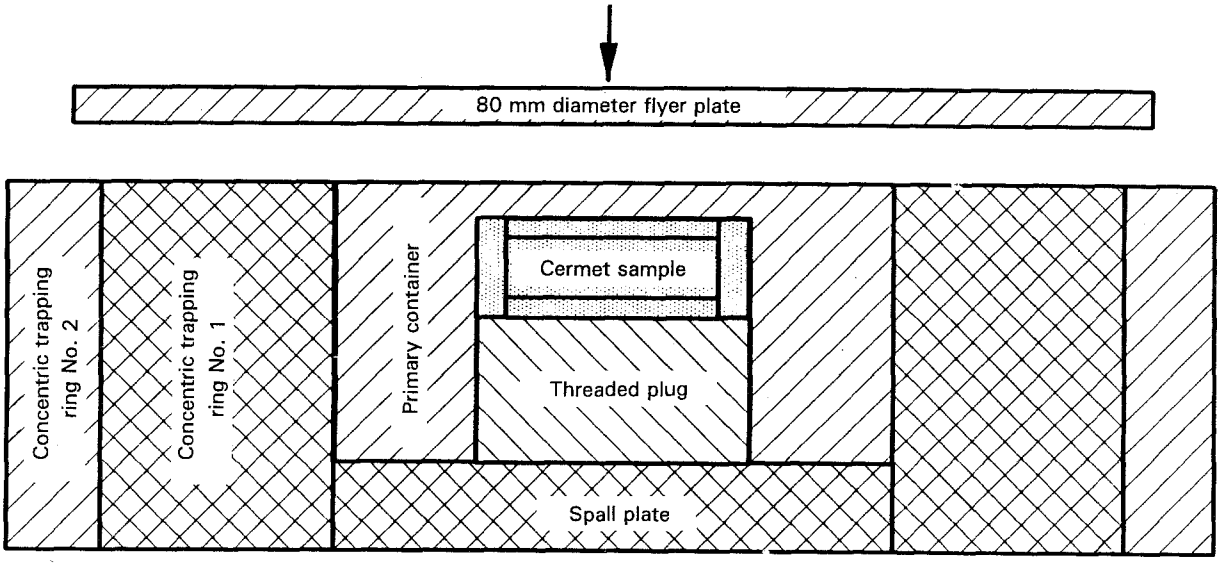

Figure 2 Shock recovery experiments were performed using an 80 mm single-stage gas gun. □, titanium 6AL–4V.

TABLE II Cermet equations-of-state used in pressure and spall calculations

Composition	Elastic EOS $km\,s^{-1}$	Plastic EOS $km\,s^{-1}$
65% B_4C–Al	$U_s = 10.63$	$U_s = 8.41 \pm 1.12\ U_p$
80% B_4C–Al	$U_s = 12.18$	$U_s = 8.82 \pm 1.07\ U_p$

(elastic), and 12.2 (plastic) to 13.5 GPa (elastic), respectively, in the 65% B_4C–Al cermet. Impact velocities of 600 and 1010 $m\,s^{-1}$ were used to produce peak shock amplitudes in the range of 7.2 (plastic) to 8.2 GPa (elastic), and 12.3 (plastic) to 14.1 GPa (elastic), respectively, in the 80% B_4C–Al cermet.

After impact the sample containers were "soft" recovered by deceleration into a water catch chamber to preserve the shock-induced microstructures and to minimize secondary collision damage. Recovery consisted of separating the flyer plate, the projectile (which carried the flyer plate) and the sample momentum trapping rings from the sample container using a "stripper can" positioned directly behind the target assembly. The stripper consisted of a thick-walled steel canister with a small exit hole in the single-closed end. The exit hole diameter was designed to permit only the sample container to pass through unimpeded. A short distance behind the stripper a "catch" chamber was located, which consisted of a series of water-soaked wool felt layers which rapidly decelerated and water-cooled the sample container. Prior experiments by Gray *et al.* [14] using this technique to recover shock-loaded highly ductile copper showed that residual strain could be maintained below 1.5%.

3.3. Sample preparation for microstructural characterization

Cermet spall samples were necessarily unconfined in the impact direction to allow spall to occur and to be measured. However, this condition also rendered them unprotected from stresses generated by deceleration into water during "soft" recovery and by secondary impacts. Consequently, spalled specimens in this study were not successfully recovered for fracture surface characterization.

"Soft" shock-recovered cermet samples were carefully extracted from their containers and prepared for microstructural characterization by TEM. Wafers nominally 250 μm thick were first sectioned from the cermets using a low-speed diamond abrasive saw. Foils, 3 mm in diameter, were ultrasonically cut from the wafers. The foils were mechanically dimpled using 3 μm diamond paste to a centre thickness of nominally 25 μm. Finally, the foils were ion-thinned at approximately − 150 °C using a 6 kV ion source at a grazing angle of 10–15 °. Characterization was performed using a Jeol 2000EX equipped with a double-tilt stage at an accelerating voltage of 200 kV.

Polished sections were also prepared for optical microscopy. Specimens were mounted so that the microstructure on planes perpendicular to the loading plane could be observed. Polishing was performed manually starting with 15 μm alumina abrasive in a water slurry followed by 6 down to 1 μm diamond paste on a flat glass plate. Extreme differences in abrasive removal rates were expected and observed between the boron carbide and aluminium phases. Consequently, only details of the boron carbide phase can be properly discerned from the polished sections using optical microscopy.

3.4. Ultrasonic velocity characterization

Ultrasonic longitudinal and shear velocities were measured in the direction of shock loading using the pulse-echo technique [15] with a 10 MHz longitudinal transducer and a 5 MHz shear transducer. Sound velocities and final densities were used to evaluate changes in the elastic constants of shock-recovered samples as compared to unshocked cermet values.

4. Results

The microstructural response of the cermets to shock loading was found to be strongly dependent on the volume fraction of boron carbide. The 80% B_4C–Al cermet samples displayed extensive, uniform fracturing during both shock-recovery and spall testing. Fragmentation was severe enough for the samples to be unsatisfactory for preparation into TEM foils, polished sections or to be used for ultrasonic velocity evaluation. Hence, the bulk of the microstructural results will concentrate on the 65% B_4C–Al cermet composition.

4.1. Shock spallation

Manganin gauge records were analysed to provide both the spall strength as a function of applied shock pressure and to establish the extent of the elastic regime for these composites in conjunction with shock-recovery results. Table III provides a comparison of spall strengths calculated based on either the elastic or the plastic EOS. For shock pressures up to 8 GPa, spall strength was found to be independent of EOS for the 65% B_4C–Al composite. Spall strength was determined to be 650 ± 30 MPa, virtually identical to the cermet quasi-static flexure strength of 624 MPa. At shock pressures between 9 to 10 GPa, the spall strength calculated using the elastic and plastic EOS diverged significantly. The spall strength from the elastic EOS dropped 20% to ca. 520 MPa, while the spall strength using the plastic EOS displayed an increase of almost 50% to ca. 950 MPa. Significantly, at the highest shock pressure studied (12–13 GPa) the elastic EOS produced a large, obviously erroneous, compressive spall strength (− 470 MPa), whereas the plastic EOS calculations yielded a spall strength of virtually zero (− 30 MPa).

In summary, an assumption of elasticity is reasonable up to shock pressures of ca. 10 GPa, for the 65% B_4C–Al cermet. The elastic spall strength was constant (± 5%) up to at least 8 GPa, but then appeared to decline by 20% at 10 GPa. At shock

TABLE III Comparative spall strengths using elastic and plastic EOS

Cermet composition	Actual impact velocity ($m s^{-1}$)	Equivalent symmetric velocity		Shock pressure		Spall strength (+ = tensile)	
		ROM ($m s^{-1}$)	Elastic ($m s^{-1}$)	ROM (GPa)	Elastic (GPa)	ROM (MPa)	Elastic (MPa)
65% B_4C–Al	616	657	582	7.2	7.9	660	620
	632	662	591	7.2	8.1	680	680
	793	828	749	9.2	10.2	955	520
	1025	1092	989	12.3	13.5	− 30	− 470
80% B_4C–Al	591	604	522	7.0	8.0	2860	1380
	865	890	780	10.5	12.0	GF[a]	GF

[a]GF = gauge failed prior to recording complete spall event.

pressures over 10 GPa plasticity clearly dominated and the spall strength fell to zero after a 12 GPa shock.

Analogous to the 65% B_4C–Al composition, the HEL of the 80% B_4C–Al cermet was expected to be ca. 80% of the HEL of polycrystalline B_4C, ca. 12 GPa. The spall strength of the 80% B_4C–Al cermet was first measured at a shock pressure of 8 GPa. Not unexpectedly, the spall strength calculated using the plastic EOS, 2900 MPa, was of questionable validity compared to the quasi-static flexure strength. However, the spall strength determined using the elastic EOS, 1380 MPa, was also much higher than expected from quasi-static flexure strength data. Spall testing at a higher shock pressure near the estimated HEL (12 GPa) resulted in gauge failure early upon release.

4.2. Shock recovery

Optical photographs (Fig. 3a and b) of shock-recovered 65% B_4C–Al cermet samples showed large blocks of intact material bounded by a low-density of periodic radial and circumferential cracks following shock loading at both 12.2 GPa (using a plastic EOS) and 6.4 GPA (using an elastic EOS), respectively. The cracking patterns were consistent with the occurrence of tensile failure caused by release waves originating from the sample circumference. High magnification optical microscopy of polished sections confirmed that the macrocracks were isolated and that the B_4C phase between the macrocracks was not visibly micro cracked.

No detectable increase in the defect density was observed in the B_4C substructure of the 65% B_4C–Al cermet by TEM following shock loading to 6.4 GPa. Fig. 4 is a low-magnification TEM bright-field which is indistinguishable from the as-received material (Fig. 1). The unchanged substructure is evidence that the B_4C phase of this composition responds elastically to shocks up to at least 6.4 GPa. The aluminium phase, on the other hand, exhibited a higher density of randomly distributed dislocation tangles following the 6.4 GPa shock. The occurrence of random dislocation tangles rather than a well-formed cellular substructure at this modest shock pressure, and for this small phase-size aluminium, was consistent with suppressed dynamic recovery [16].

The microstructure of the 65% B_4C–Al cermet following shock loading to 12.2 GPa resembled the

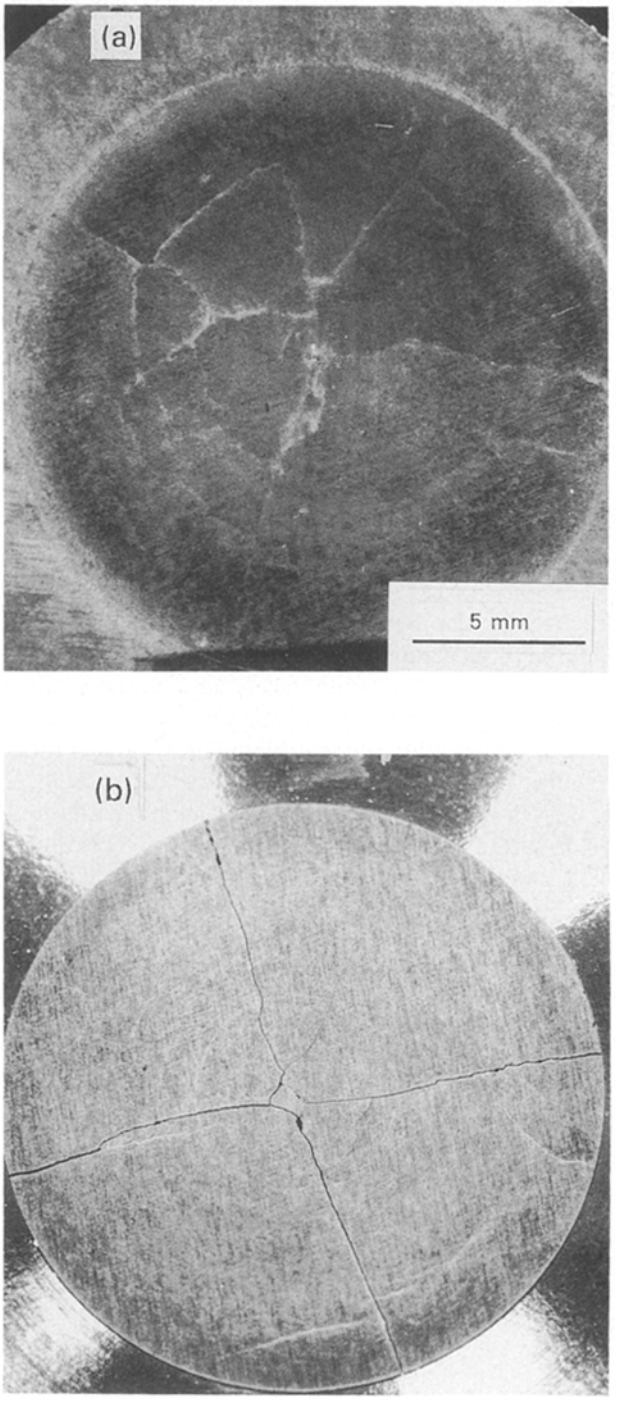

Figure 3 Optical photographs of shock-recovered 65% B_4C–Al cermet samples showing large regions of intact material bounded by periodic radial and circumferential cracks. (a) 12.2 GPa and (b) 6.4 GPa.

Figure 4 Low magnification TEM of the general microstructure of 65% B_4C–Al following a shock of 6.4 GPa.

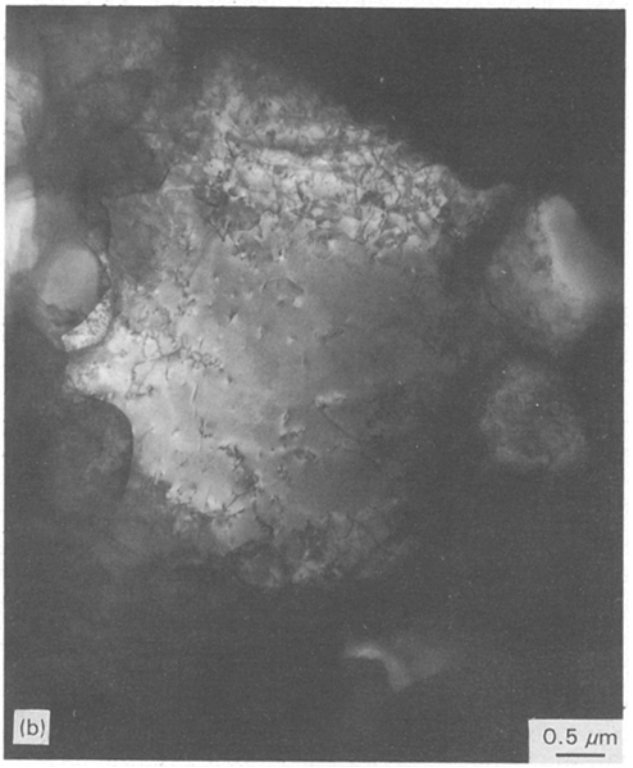

Figure 5 (a) and (b) High magnification TEM of 65% B_4C–Al after a shock of 12.2 GPa revealing that plastic deformation had occurred in some B_4C grains.

6.4 GPa case under low-magnification TEM examination, where the majority of the B_4C grains remained essentially free of defects. However, high magnification TEM (Fig. 5a and b) revealed that a small fraction of the B_4C grains were clearly plastically deformed. Generally, the dislocation debris was concentrated near the grain facets and corners. This distribution of defects was consistent with the existence of deformation compatibility constraints in these regions. In addition to dislocation debris, some B_4C grains showed evidence of fine stacking faults and deformation twins. Fig. 6a and b are two TEM bright-field images of the same area under different beam conditions which illustrate details of the twins and stacking faults. Fig. 6a is oriented near a $[\bar{1}\,1\,0\,1]$ zone-axis. Fig. 6b is tilted off the zone-axis putting the twins out of contrast, but changed the fine fault lines shown in Fig. 6a into resolved stacking faults. Fig. 7 is a bright-field micrograph and a corresponding selected-area diffraction pattern (SAD) of deformation twins in a B_4C grain. Analysis of the $[\bar{1}\,1\,0\,1]$ matrix SAD pattern shows that the twins lay on the $(0\,1\,\bar{1}\,\bar{1})$ twin plane. Analysis of additional twins concluded that they were all the same twin type. This twin plane is identical to that found previously by Kim *et al.* [17] in statically and dynamically deformed B_4C–Al cermets.

4.3. Ultrasonic and elastic properties

Ultrasonic velocity measurements of the unshocked cermets were found to be nearly constant as a function of orientation demonstrating these cermets to be macroscopically isotropic, in contrast to continuous fibre- or planar laminate-reinforced composites. Elastic moduli calculated from the ultrasonic velocities are plotted as a function of B_4C volume fraction in Fig. 8. Voigt [18] and Reuss [19] composite modulus models are also presented and represent the two anisotropic extremes of dual-phase composite behaviour. The Voigt model [18] assumes iso-strain conditions

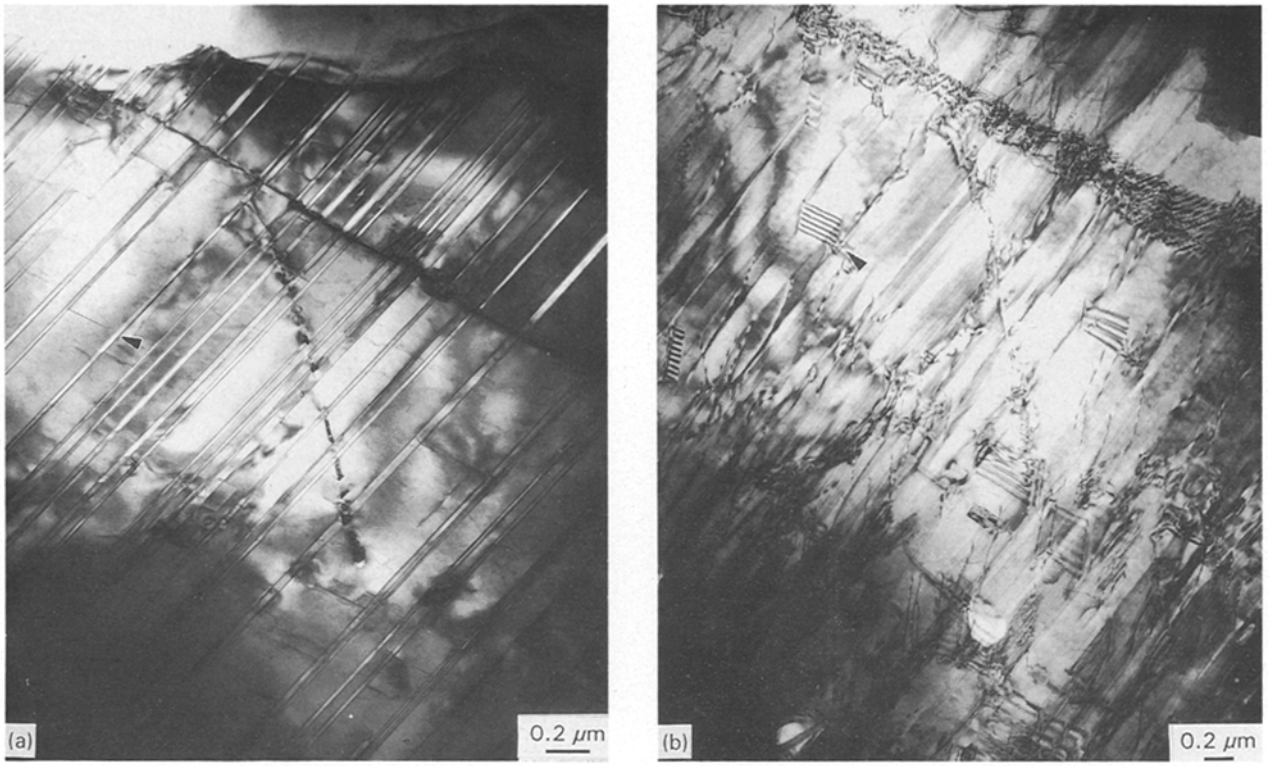

Figure 6 TEM bright-fields of the same area under different beam conditions revealing details of deformation twins and stacking faults. (a) was oriented near a $[\bar{1}\,1\,0\,1]$ zone-axis; (b) was tilted off the zone-axis to resolve the stacking faults.

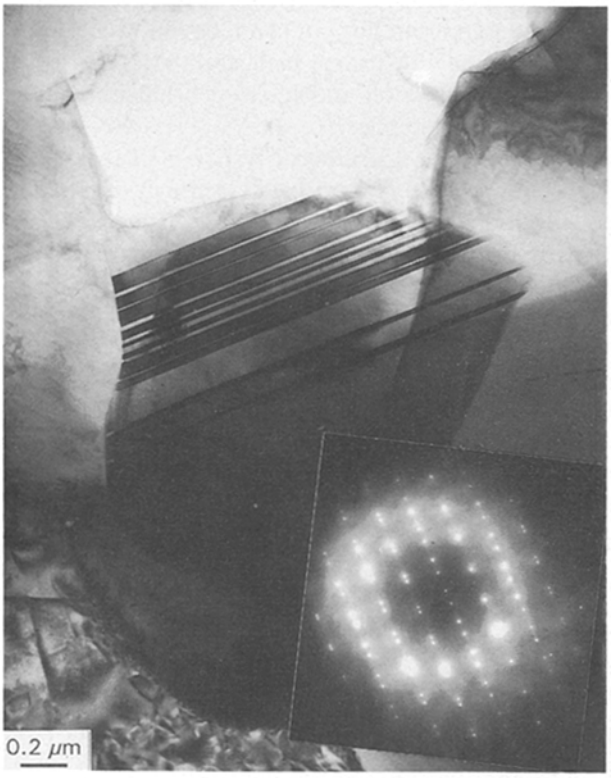

Figure 7 Bright-field and selected area diffraction (SAD) TEM of $(0\,1\,\bar{1}\,\bar{1})$ deformation twins in the B_4C–Al cermet shock-loaded to 12.2 GPa.

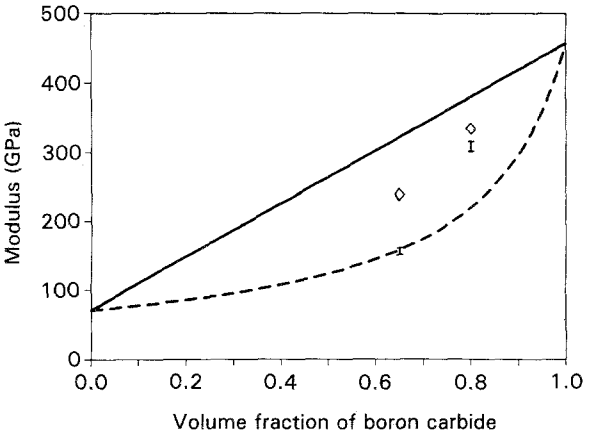

Figure 8 Elastic moduli calculated from ultrasonic velocities plotted as a function of B_4C volume fraction. Voigt [18] (————; iso-strain) and Reuss [19] (- - - ; iso-stress) composite modulus models are also presented in addition to the secant moduli obtained from quasi-static compressive stress–strain curves at 1% strain. ◇, ultrasonic modulus; I, secant modulus at 1% strain.

are maintained in both phases and predicts a composite elastic modulus based upon a rule-of-mixtures of the moduli of the individual phases and their volume fractions. The Reuss model [19] assumes equal stress conditions are maintained in both phases so that the composite modulus is calculated as:

$$E_c = \frac{E_1 E_2}{V_1 E_2 + V_2 E_1} \quad (1)$$

Where E_c = composite elastic modulus; V_i = volume fraction of phase 1 or 2, and E_i = elastic modulus of phase 1 or 2. The ultrasonic moduli of both compositions were closely approximated by averaging the Voigt and Reuss predictions together as suggested by Hill [20] for isotropic composites. Fig. 8 shows the secant moduli obtained from quasi-static compressive

TABLE IV Shock-recovered ultrasonic and elastic properties

Property	As-received	Shock pressure	
		6.4 (GPa)	12.2 (GPa)
C_l (km s^{-1})	10.63 ± 0.02	10.01 ± 0.01	9.63 + 0.08
C_s (km s^{-1})	6.24 ± 0.01	6.01 ± 0.01	5.68 ± 0.07
Young's modulus (GPa)	247	226	199

stress–strain curves at 1% strain, which is close to the failure strain of polycrystalline boron carbide [21]. The secant modulus of 65% B_4C–Al cermet dropped 40% to a value equivalent to a Reuss solid. However, the secant modulus for the 80% B_4C–Al cermet declined only by 10% from its initial ultrasonic value.

Ultrasonic characterization of intact portions of the shock-recovered 65% B_4C–Al samples indicated a steady decay in both the longitudinal and shear velocities (C_l, C_s) with shock pressure as summarized in Table IV. Declines of approximately 4% and 9% from as-received velocities were observed for shock pressures of 6.4 and 12.2 GPa, respectively. The density of the ultrasonic specimens were measured using Archimedes method and were found to be 99.9% of the unshocked cermet density for both shock pressures. Therefore, the observed velocity changes were not easily attributed to a loss in density in the shock-recovered samples. A corresponding decay in the Young's modulus towards Reuss solid behaviour was calculated for the shock-loaded 65% B_4C–Al cermet. Reductions of 10 and 20% from the as-received Young's modulus were calculated for the 6.4 and 12.2 GPa shocks, respectively.

5. Discussion

5.1. Shock spallation

Shock-spallation tests measured not only the spall strength as a function of applied shock pressure, but also provided information on the nature and magnitude of the elastic limit in the shock regime. Results for the 65% B_4C–Al cermet indicated that spall strength was nearly equal to the quasi-static flexure strength up to shock pressures of about 10 GPa, or approximately 65% of the HEL of polycrystalline B_4C [2]. However, at a higher shock pressure of 12 GPa, a fully plastic EOS appeared to dominate (which also resulted in a calculated spall strength near to zero). Hence, an HEL of between 10 and 12 GPa was estimated for the 65% B_4C–Al cermet based on this evidence. This estimate represents an "upper limit" value for the composite HEL and corresponds to the onset of plasticity within the B_4C-substructure as evidenced by the results of the shock-recovery experiments. By analogy, an "upper limit" HEL of 12 GPa (80% of the HEL of polycrystalline B_4C) was predicted for the 80% B_4C–Al cermet.

An alternate "yield-stress-based" estimate of the HEL can be made by assuming that the rate-dependent yield behaviour of the cermets observed in quasi-static and split Hopkinson pressure bar (SHPB) compression can be extended to shock wave strain rates. The stress state developed in uniaxial compression has been compared to the uniaxial stress–strain state produced by shock loading using the following equation [22].

$$\mathrm{HEL} = (1 - \nu)/(1 - 2\nu)Y \quad (2)$$

where ν is Poisson's ratio and Y is the uniaxial compression yield strength at a strain rate equivalent to an elastic shock wave. The strain-rate dependence of the uniaxial compression yield strength can be described empirically by [22].

$$\sigma = \sigma_0(\dot{\varepsilon}/\dot{\varepsilon}_0)^m \quad (3)$$

where σ is the stress, $\dot{\varepsilon}$ is the strain rate, and σ_0, $\dot{\varepsilon}_0$ and m are constants. At room temperature, m has been measured as 0.017 and 0.001 between 10^{-3} and 2000 s^{-1} for the 65% and 80% B_4C–Al cermets, respectively [21]. Assuming that a maximum strain rate of 10^6 s^{-1} occurred during the elastic portion of the shock wave, and using the compressive strengths listed in Table I, then the "yield-stress-based" estimates of HEL were 4.0 and 6.9 GPa for the 65 and 80% B_4C–Al cermets, respectively. These values represent "lower limit" estimates for the composite HEL. The 40–60% difference between the "upper limit" and "lower limit" estimates suggested: 1. the transition from elastic to fully plastic behaviour in both phases of the cermets occurred over a broad stress regime; and 2. the rate dependence of the "yield stress" of composites were not monotonic and could not be simply extrapolated from moderate to very high strain rates due to the complex deformation and fracture behaviour of the continuous brittle phase.

In general, the mechanical response of these very high ceramic content composites is clearly dominated by the highly-elastic, strain-rate-insensitive and extremely brittle boron carbide phase compared to the low-flow-stress, strain-rate-sensitive and extremely ductile aluminium phase.

5.2. Shock recovery

Several factors were considered important for maintaining the integrity of these shock-loaded cermets: 1. confinement provided by an impedance-matched metal container limited tensile strains in the sample and provided protection from secondary impacts during recovery; 2. intricate "soft"-shock recovery techniques originally developed for ductile metals were effectively adapted for these materials; and 3. high fracture toughness, provided by the ductile aluminium phase, suppressed crack propagation in the B_4C phase.

The extent of extraneous cracking in the "soft"-shock-recovered cermets was strongly dependent on both the magnitude of the applied shock pressure and the composition of the cermet. Shock loading the 80% B_4C–Al cermet between the "upper limit" and "lower limit" estimates of the HEL always produced relatively severe fragmentation indicating that late-time crack propagation within the brittle B_4C phase was insufficiently suppressed by the nominal 20 vol %

ductile aluminium phase present. In contrast, the nominal 35 vol % aluminium content of the 65% B_4C–Al cermet was sufficient to suppress extraneous crack propagation in the B_4C phase at shock pressures greater than the "upper limit" estimate for the HEL.

Intact recovery was essential for studying the microstructural changes produced by the shock, especially remnant defects from plastic flow. Hence, in the case of the 80% B_4C–Al where fragmentation apparently occurred following the applied shock, the authors did not attempt to attribute defects contained in the fragments to the shock loading process. These defects could have easily been generated during the fragmentation process. Therefore exceptional care must be taken when assessing defect generation in brittle materials prescribed to shock loading.

An important finding was made by shock-loading the 65% B_4C–Al cermet to 12 GPa (above the estimated "upper limit" HEL). TEM was used to observe dislocation debris, fine deformation twins and stacking faults which were evidence of plastic deformation within the B_4C phase. To the authors' knowledge detection of these defects in single-phase B_4C following controlled shock-loading at room temperature have not been made due to material fragmentation.

The decay in the ultrasonic velocities and corresponding elastic moduli of the shock-loaded 65% B_4C–Al cermet suggested the operation of one or more of the following mechanisms:

1. Progressive microcracking (i.e. damage starting with the weakest) of the B_4C grain boundaries or the B_4C–Al interfaces. Microcracking interferred with the propagation of ultrasonic waves by causing attenuation and a lowering of the sound velocity. Microcracking is also known to degrade the stiffness of materials.
2. Phase rearrangement and segregation within the microstructure. These cermets are specifically fabricated to be macroscopically isotropic, but at the microstructural level strain was not accommodated uniformly. The B_4C grains remained relatively rigid during cermet deformation, although individual grains may have rotated and slid in conjunction with the microcracking referred to above. Equally important, applied strain was primarily concentrated in the soft aluminium phase which flowed to accommodate stress gradients. Hence, the two phases could segregate and their macrostructures rearrange in response to loading. This would result in the development of an anisotropic mechanical response.
3. Finally, the aluminium phase could undergo very large localized deformations as mentioned above, resulting in crystallographic "texturing" which also leads to an anisotropic mechanical response.

All the conditions stated above could reduce ultrasonic velocities and the corresponding elastic stiffness in the loading direction without measurably reducing the material's bulk density.

6. Summary

This study demonstrated that a ductile phase properly combined with a high performance, brittle ceramic phase could reduce fracturing associated with dynamic loading without sacrificing strength. Specifically, the aluminium phase in these cermets appeared to maintain the integrity of the composites to varying degrees by resisting the propagation of cracks throughout the brittle B_4C substructure.

1. Successful recovery of the 65% B_4C–Al cermet was largely due to its high fracture toughness and tensile strength, but also because of the advanced recovery techniques employed. Use of high tensile strength containment and momentum trapping components fabricated from nearly impedance-matched materials was essential to minimize fragmentation. Observations of radial and circumferential cracking argued that imperfect interfaces and impedance mis-matching conditions still existed and were virtually impossible to eliminate.
2. The microstructure of the B_4C phase in the 65% B_4C–Al cermet appeared largely unchanged following both a 6.4 and a 12.2 GPa shock using low-magnification TEM. This inferred an elastic mechanical response for the B_4C phase (if not the entire composite) up to shock pressures of 12 GPa. However, higher magnification TEM examination of the B_4C phase of the 12.2 GPa shocked sample revealed dislocation activity and fine twins in a small fraction of the B_4C grains. This provided evidence that the HEL of the B_4C phase (corresponding to the "upper limit" HEL of the composite) had been exceeded with a 12 GPa shock.
3. Spall-strength calculations, using both elastic and plastic equations-of-state, for the 65% B_4C–Al cermet also indicated that an assumption of elasticity was reasonable up to shock pressures of ca. 10 GPa or ca. 65% of the HEL of polycrystalline B_4C. The spall strength in this elastic regime was ca. 650 MPa, nearly identical to the quasi-static flexure strength. At shock pressures over 10 GPa, plasticity clearly dominated and the spall strength fell essentially zero with a 12 GPa shock.
4. The spall strength of the 80% B_4C–Al cermet was successfully measured at only one shock pressure (8 GPa) between the "upper limit" and "lower limit" estimates of the HEL. The spall strength at this shock pressure was anomalously high (1400 MPa), being over twice the quasi-static flexure strength.
5. The excellent spall strengths exhibited by these cermets following strong shock loading proved that they are viable candidates for impact applications. The 65% B_4C–Al cermet should be particularly useful in long-duration or multiple shock environments. The spall strength of the 80% B_4C–Al cermet was also quite high compared to polycrystalline B_4C; however, due to extraneous fragmentation the integrity of this cermet composition could not be adequately maintained under multiple-impact applications or during long-duration shock events.

Acknowledgement

This work was supported by the DARPA Balanced Technology Initiative and the Army Research Office.

Work was performed under the auspices of the US Department of Energy. Special thanks to Professor Ilhan Aksay and Dr Dave Millius for providing their unique materials and associated property data; Walt Wright, Carl Trujillo, Walt Bast and Scott Gibbs for their assistance preparing and testing these materials; and Sun Ig Hong and Anna Zurek for reviewing the manuscript.

References

1. D. E. GRADY and M. E. KIPP, *Int. J. Rock. Mech. Min. Sci. Geomech. Abstr.* **16** (1979) 293.
2. M. E. KIPP and D. E. GRADY, "Shock compression and release in high-strength ceramics" (Sandia National Laboratory, SAND89-1461, UC-704, July 1989).
3. G. T. GRAY III, "Shock-wave and high strain-rate phenomena in materials", edited by M. Meyers, L. Murr and K. Staudhammer (Mercel Dekker, New York, 1992) p. 899.
4. Y. SYONO, T. GOTO, Y. NAKAGAWA and M. KITAMURA, in "High pressure research", edited by M. H. Manghnani and S. Akimoto (Academic Press, New York, 1977) p. 477.
5. D. E. GRADY, *ibid.* p. 389.
6. R. JEALOZ, *J. Geophysical Res.* **85** (1980) 3163.
7. J. A. BRUSSO, D. E. MIKKOLA, J. E. FLINN and P. V. KELSEY, *Scripta Metall.* **22** (1988) 47.
8. D. M. VANDERWALKER and W. J. CROFT, *J. Mater. Res.* **3** (1988) 761.
9. L. LOURDO, A. LINDFORS and M. MEYERS, *Dymat*88 *J. De Physique Colloque C3 Supplement* #9 **49** (1988) 133.
10. D. MILLIUS, Private communication (1989).
11. T. P. LIDDIARD Jr, in "Fourth symposium on detonation", edited by USNOL (US Government Printing Office, Washington, DC 1965) p. 214.
12. L. M. BARKER and R. E. HOLLENBACH, *J. Appl. Phys.* **41** (1970) 4208.
13. V. I. ROMANCHENKO and G. V. STEPANOV, *Zhur. Prik. Mekh. Tekh. Fia.* **4** (1980) 141.
14. G. T. GRAY III, P. S. FOLLANSBEE and C. E. FRANTZ, *Mater. Sci. Engng.* **A111** (1989) 9.
15. E. P. PAPADAKIS, in "Physical acoustics principles and methods", Vol. 12, edited by W. P. Mason and R. N. Thurston (Academic Press, New York, 1976) Ch. 5.
16. G. T. GRAY III and J. C. HUANG, *Mater. Sci. Engng.* **A1415** (1991) 21.
17. G. H. KIM, M. SARIKAYA, D. L. MILLIUS and A. K. AKSAY, in "Proceedings of the 47th Annual Meeting of the Electron Microscopy Society of America", edited by G. W. Bailey (San Francisco Press, CA, 1989) p. 562.
18. W. VOIGT, in "Lehrbuch der kristallphysik" (Teubner, Leipzig, Germany, 1928) p. 739.
19. A. REUSS, *Z. Angew. Math. Mech.* **9** (1929) 49.
20. R. HILL, *Proc. Phys. Soc London* **A65** (1952) 349.
21. W. R. BLUMENTHAL, Unpublished work.
22. P. S. FOLLANSBEE, in "Shock compression of condensed matter – 1989", edited by S. Schmidt, J. N. Johnson and L. Davidson (Elsevier, New York, 1990) p. 349.

Received 6 May 1993
and accepted 25 February 1994